van der Waals epitaxy of Ge films on mica

A. J. Littlejohn, Y. Xiang, E. Rauch, T.-M. Lu, and G.-C. Wang

Citation: Journal of Applied Physics **122**, 185305 (2017);
View online: https://doi.org/10.1063/1.5000502
View Table of Contents: http://aip.scitation.org/toc/jap/122/18
Published by the American Institute of Physics

Sharp, quick summaries illuminating the latest physics research
Sign up for FREE!
AIP Publishing

JOURNAL OF APPLIED PHYSICS **122**, 185305 (2017)

van der Waals epitaxy of Ge films on mica

A. J. Littlejohn, Y. Xiang, E. Rauch, T.-M. Lu, and G.-C. Wang
Department of Physics, Applied Physics and Astronomy, and Center for Materials, Devices, and Integrated Systems, Rensselaer Polytechnic Institute, 110 8th Street, Troy, New York 12180, USA

(Received 16 August 2017; accepted 14 October 2017; published online 14 November 2017)

To date, many materials have been successfully grown on substrates through van der Waals epitaxy without adhering to the constraint of lattice matching as is required for traditional chemical epitaxy. However, for elemental semiconductors such as Ge, this has been challenging and therefore it has not been achieved thus far. In this paper, we report the observation of Ge epitaxially grown on mica at a narrow substrate temperature range around 425 °C. Despite the large lattice mismatch (23%) and the lack of high in-plane symmetry in the mica surface, an epitaxial Ge film with [111] out-of-plane orientation is observed. Crystallinity and electrical properties degrade upon deviation from the ideal growth temperature, as shown by Raman spectroscopy, X-ray diffraction, and Hall effect measurements. X-ray pole figure analysis reveals that there exist multiple rotational domains in the epitaxial Ge film with dominant in-plane orientations between Ge$[\bar{1}10]$ and mica[100] of $(20n)^\circ$, where $n = 0, 1, 2, 3, 4, 5$. A superlattice area mismatch model was used to account for the likelihood of the in-plane orientation formation and was found to be qualitatively consistent with the observed dominant orientations. Our observation of Ge epitaxy with one out-of-plane growth direction through van der Waals forces is a step toward the growth of single crystal Ge films without the constraint in the lattice and symmetry matches with the substrates. *Published by AIP Publishing*. https://doi.org/10.1063/1.5000502

I. INTRODUCTION

Germanium exhibits several properties, which have enabled it to become a prevalent material in many semiconductor-based devices including optoelectronics. Its 0.67 eV bandgap places it in the infrared regime, allowing Ge to be used for IR photodetection,[1–3] while its exceptional mobility, higher than that of Si, makes it a critical component in integrated circuits and transistors. Furthermore, because Ge's lattice structure matches closely with that of GaAs, Ge has served as the substrate for the epitaxial growth of GaAs for the use in LEDs[4,5] and high-efficiency solar cells.[6,7] The growth of high quality semiconductor films such as Ge both for use in electronic and optoelectronic devices as well as for the substrates for the subsequent growth of semiconductor heterostructures is of paramount importance.

For the growth of large area semiconductor films needed for applications including solar arrays, single crystal substrates are often too expensive to make commercial-scale processes economically viable.[8] In addition, the use of cheaper biaxial or amorphous substrates results in the growth of a lower quality film with a high density of random-angle grain boundaries, which translates to diminished minority carrier lifetime[9] and increased recombination,[10,11] resulting in poorer efficiency.[12] Growth via van der Waals epitaxy (vdWE, i.e., epitaxial growth on a vdW substrate) may be one potential solution.[13–17] The atoms that comprise vdW materials (also referred to as 2D or layered materials) exhibit strong in-plane chemical bonding through the sharing of electrons, but weak physical attraction between layers via the van der Waals force. Thus, when cleaved perpendicular to the layered direction, the surface of a vdW material is atomically smooth and free of dangling bonds, allowing for the growth of crystalline films without the constraint of lattice-matching as is required for traditional 3D/3D epitaxial growth. The resultant film should contain little to no strain.

Muscovite mica ($K_2O{\cdot}Al_2O_3{\cdot}SiO_2$) is one such layered material which has been studied as a template for vdWE growth of semiconductor films.[14,17,18] In addition to being a layered material, mica is stable up to about 700 °C,[19] highly flexible, durable, inexpensive, and thin layers can easily be cleaved from the bulk material revealing a surface that has over 1 cm^2 step-free areas.[20] By growing high quality Ge films on mica, one could produce a flexible, durable template for high efficiency electronic and optoelectronic devices by a method which is relatively inexpensive.

Interestingly, the literature reports that growth of single-orientation Ge film on mica by vdWE is not possible.[21] In fact, only at high temperatures (above 800 °C) were oriented grains (fiber texture) formed, but not an epitaxial single crystal. In this report, we present the vdWE growth of epitaxial Ge(111) film deposited on mica substrates by thermal evaporation. By finely varying the substrate temperature during deposition and annealing in the range of 300–500 °C, we have found a window for Ge epitaxy, with the optimal temperature for Ge crystallinity at 425 °C, previously unreported in the literature. Also, the temperature is much lower than the literature reported temperature for Ge fiber texture films grown on mica.[21] We characterize the surface morphology of Ge films using atomic force microscopy (AFM) and scanning electron microscopy (SEM), the atomic structure and epitaxial relationship using Raman spectroscopy, X-ray diffraction (XRD), XRD reciprocal space mapping and XRD pole figure analysis, the near-surface texture using reflection high energy electron diffraction (RHEED), and the charge

carrier mobility by Hall effect measurements. With the success of our Ge film grown on mica at a practical temperature, we anticipate that other nonlayered elemental or alloyed materials can be grown on mica via van der Waals epitaxy. This enables applications in flexible electronics and optoelectronics and greatly broadens the choice of materials.[22]

II. EXPERIMENTAL

The Ge film deposition on mica is similar to that used in a previous study of $Ge_{1-x}Sn_x$ films.[23] Here we present a brief summary. Ge films were grown via normal incidence physical vapor deposition onto air-cleaved single crystal mica (001) substrates (mica grade V-4, SPI Supplies, 75 mm × 25 mm × 0.26 mm) in a vacuum chamber pumped to a base pressure on the order of 10^{-8} Torr. Chamber pressure reached mid 10^{-7} Torr during deposition. Ge pellets (99.9% pure, Kurt J. Lesker Co.) were placed in an alumina-coated tungsten basket mounted approximately 30 cm below the substrates. Flux rates (1.5–2.5 Å s^{-1}) and deposited film thickness were monitored by a quartz crystal microbalance mounted adjacent to the substrate housing unit and calibrated using cross-section SEM images. For each sample, ∼80 nm of Ge was deposited with the substrate heated to 300, 350, 400, 425, 450, and 500 °C, with uncertainties of approximately ±5 °C. Samples were subsequently annealed at the deposition temperature *in situ* for 1 h. This has previously been shown to improve uniformity and enhance the crystallization of Ge films.[24]

SEM images were taken on a Zeiss Supra 55 SEM using a beam energy of 2.5 keV and a 30 μm aperture. 1 μm × 1 μm AFM images were taken using a Park Systems XE7 Scanning Probe Microscope in the non-contact mode at a selected frequency of approximately 163 kHz, using a cantilever with a spring constant of approximately 36.0 N m^{-1}. Raman spectra were collected using a Renishaw 2000 Raman spectrometer in backscattering geometry with a ∼10 mW, 514 nm excitation source focused down to a spot size of about 5 μm using a 50× optical lens. The spectrometer has a resolution of about 0.7 cm^{-1} using a 2400 g/mm grating and spectra were integrated for 40 s. Data collected from a single crystal Ge(111) wafer (MTI) were used as a reference. A Bruker D8 Discover X-ray diffractometer (Cu Kα, λ = 1.5406 Å) was used to obtain XRD scans. Coarse survey scans utilized a 0.01° step size, while fine scans were collected with 0.001°/step. Reciprocal space maps (RSMs) and $\theta/2\theta$ scans were taken with a four-bounce Ge(220) monochromator in the incident optics to remove the Kα_2 and Kβ signals and a 0.1 mm slit in the diffracted optics to enhance resolution. 0.6 mm slits were used in the incident and diffracted optics for the collection of pole figures to achieve maximum intensity and simultaneously extract data from the substrate and film. A 2° step size was used for both ϕ and χ in collection of pole figures. Peak parameters were extracted from Gaussian fits obtained using ORIGIN software. The RHEED pattern was projected on a phosphor screen mounted on a 6-in. flange in a high vacuum chamber (10^{-8} Torr). The electron beam was generated from an electron gun (model RDA-003G) using an emission current of 48 μA and accelerated at 20 keV. The electron beam had a glancing incident angle of <1° on the sample near surface and was perpendicular to the phosphor screen. The system was calibrated[25] using a RHEED pattern of a single crystal CdTe film with a known lattice constant of 6.48 Å. The sample holder is capable of rotating azimuthally around an axis perpendicular to the sample surface with a step increment of 1.8° by a high vacuum compatible step motor. This allows RHEED patterns to be observed at different azimuthal angles. The RHEED pattern on the phosphor screen was captured by a digital camera positioned outside the vacuum chamber. Hall mobility measurements were made with an Accent HL5500PC Hall Effect Measurement System using a current of 1 μA and under a magnetic field of 5180 Gauss. To create electrical contacts, indium was secured to the surface of each film at room temperature (and without annealing) by applying pressure.

III. RESULTS AND DISCUSSION

A. Temperature-dependent morphology evolution of Ge films on mica substrates

Figure 1 shows SEM images and AFM scans of Ge/mica films grown at increasing temperatures ranging from 300 to 500 °C. Each film is continuous and composed of cluster features indicative of the Volmer-Weber (VW) growth mode.[26] Owing to enhanced adatom diffusion resulting from higher kinetic energy, the cluster diameter increases with substrate temperature. Above 400 °C, smaller clusters are observed in addition to the larger features, giving rise to an apparent bimodal distribution. Height-height correlation analysis (HHCA) was utilized to quantify the surface roughness of each film and characterize the temperature-dependent morphology evolution. The height-height correlation function is given by

$$H(r) = \langle [h(r) - \langle h(0) \rangle]^2 \rangle, \tag{1}$$

where $h(r)$ and $h(0)$ are the surface heights at positions r and reference position $r = 0$, respectively.[27] Root-mean-square roughness, ω, describes the vertical surface roughness at large distances and is the square root of $(H(r)/2)$. Lateral correlation length, ξ, quantifies the lateral dimension of surface features. Table I presents roughness quantities extracted for each film.

Consistent with qualitative images collected by SEM and AFM, both ω and ξ show positive trends with increasing growth temperature, indicating temperature-enhanced kinetic roughening.[28] The films' morphologies appear consistent with both pure Ge and $Ge_{0.95}Sn_{0.05}$ films grown on bulk, non-vdW CaF_2 substrates.[23,24]

B. Temperature-dependent crystallinity evolution of Ge films on mica substrates

1. Raman spectroscopy

In a Raman spectrum taken of a sample composed of many microcrystalline domains, each domain interacts with the excitation source and produces its own spectrum. Slight

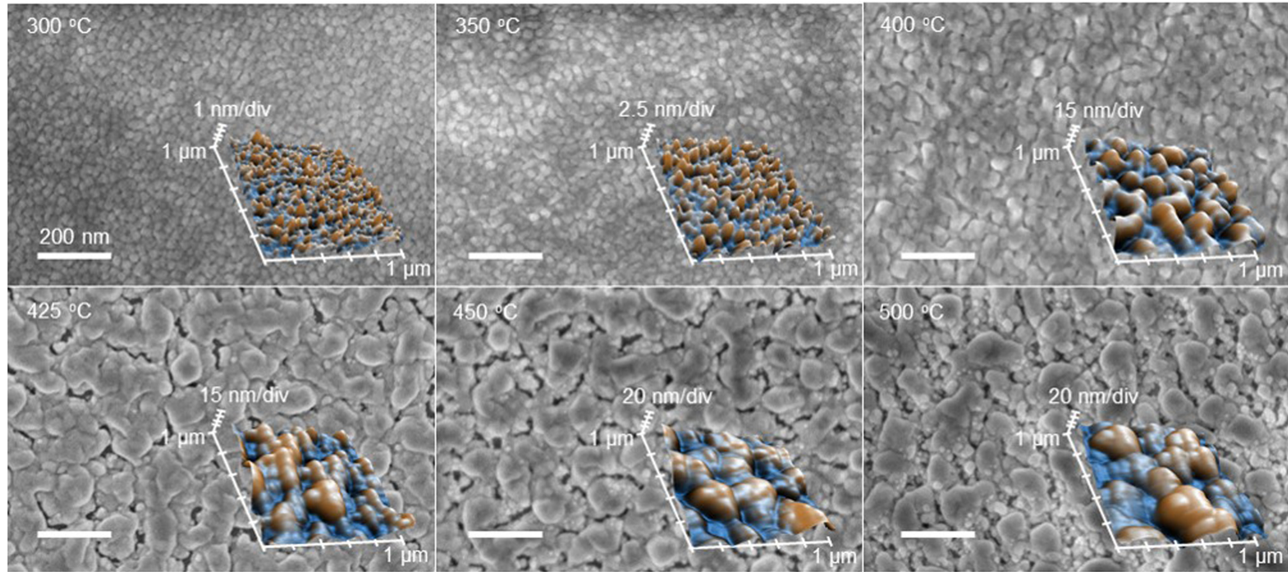

FIG. 1. Temperature-dependent morphology evolution of Ge films on mica. Ge films were grown on mica at 300, 350, 400, 425, 450, and 500 °C. The scale bar in each SEM image is 200 nm. 3D 1×1 μm AFM images are superimposed on the SEM images.

differences in atomic spacing, defect density, and microcrystalline size between domains will produce differences in the spectra. The spectrum collected for the entire ensemble of domains is the sum of these spectra and exhibits a wider (larger full-width-at-half-maximum, FWHM), weaker (lower intensity) profile relative to a bulk single crystal because of this anisotropy. Thus, a greater intensity and smaller FWHM are indicative of one or more of: (i) improved homogeneity; (ii) decreased defect density; and (iii) larger domains. Each is in turn indicative of improved crystalline quality.

Raman spectra were collected for each film as well as for a single crystal Ge wafer for reference. The spectrum collected for the Ge wafer is shown in Fig. S1 (supplementary material). One peak corresponding to the transverse optical (TO) mode is observed, centered at $300.8\,\mathrm{cm}^{-1}$, in good agreement with reports from others.[29,30] It has an amplitude and FWHM of 1.72×10^4 counts and $4.7\,\mathrm{cm}^{-1}$, respectively. Figures 2(a) and 2(b) show the Raman spectra of each film and the quantitative parameters extracted therefrom. Each peak is centered at $299.3 \pm 0.9\,\mathrm{cm}^{-1}$, in close correspondence to the peak collected for the single crystal Ge wafer. No spectrum exhibits a peak at $270\,\mathrm{cm}^{-1}$, revealing that none of the films contain appreciable amorphous content.[30,31] A clear relation between growth temperature and Raman peak amplitude is observed. The intensity (filled red triangles) is weakest in the films grown at the lowest temperatures (300 °C and 350 °C), increases with temperature maximizing at 425 °C, and then decreases in the higher temperature films (450 °C and 500 °C). The peak FWHMs (filled blue squares) follow the opposite trend, minimizing at 425 °C. Polynomial fits are included in Fig. 2(b) to guide the eye. Each trend indicates optimal crystalline quality in the 425 °C film, although the FWHM of about $8.4\,\mathrm{cm}^{-1}$ exhibited by this film is still considerably larger than that collected for the Ge wafer. This reveals that even the best film obtained by vdWE on a mica substrate is not of single crystal quality.

TABLE I. Quantification of temperature-dependent morphology evolution in Ge/mica films. Surface roughness parameters extracted from height-height correlation analysis of AFM scans. Uncertainties in ω values are approximately ±5%.

Growth Temp. (°C)	300	350	400	425	450	500
ω (nm)	0.6	1.8	10.4	8.0	13.3	13.4
ξ (nm)	22 ± 6	28 ± 6	49 ± 3	88 ± 8	112 ± 13	114 ± 15

2. Determination of out-of-plane orientation by XRD

X-ray diffraction theta/two-theta (XRD $\theta/2\theta$) scans were collected for each film as a second confirmation of the optimal growth temperature to achieve crystallinity. Mica exhibits a monoclinic structure (space group No. 15, C 2/c) with bulk lattice constants $a = 5.225$ Å, $b = 9.163$ Å, and $c = 20.275$ Å, $\alpha = \gamma = 90°$, $\beta = 95.78°$ [JCPDS No. 00-046-0741]. The interplanar spacing, d_{hkl}, is given by

$$d_{hkl} = \left\{ \frac{1}{\sin^2\beta} \left(\frac{h^2}{a^2} + \frac{k^2 \sin^2\beta}{b^2} + \frac{l^2}{c^2} - \frac{2hl\cos\beta}{ac} \right) \right\}^{-1/2}. \quad (2)$$

Germanium has a diamond cubic crystal structure (space group No. 226, $Fm\overline{3}m$) with bulk lattice constants $a = b = c = 5.658$ Å, $\alpha = \beta = \gamma = 90.0°$ [JCPDS No. 00-004-0545]. Figures 3(a) and 3(b) show $\theta/2\theta$ survey scans for the Ge/mica sample grown at 425 °C and bare mica, respectively. Strong mica (00l) peaks for $l = 2n$ with integer $n = 2, 3, \ldots, 7$ are observed in this angular range and highlighted in Fig. 3(b). In addition to the primary peak (Cu Kα), each mica(00l) exhibits peaks due to Cu Kβ, W Lα_1, and W Lβ_1 as is common for spectra of strongly diffracting single crystals collected with an aging X-ray source. No other (hkl) peaks are observed; thus, the out-of-plane orientation of mica is confirmed to be (001). Figure 3(c) shows zoomed-in scans of the region of interest for each Ge film. Each shows one strong peak located at approximately $2\theta = 26.78°$ attributed to

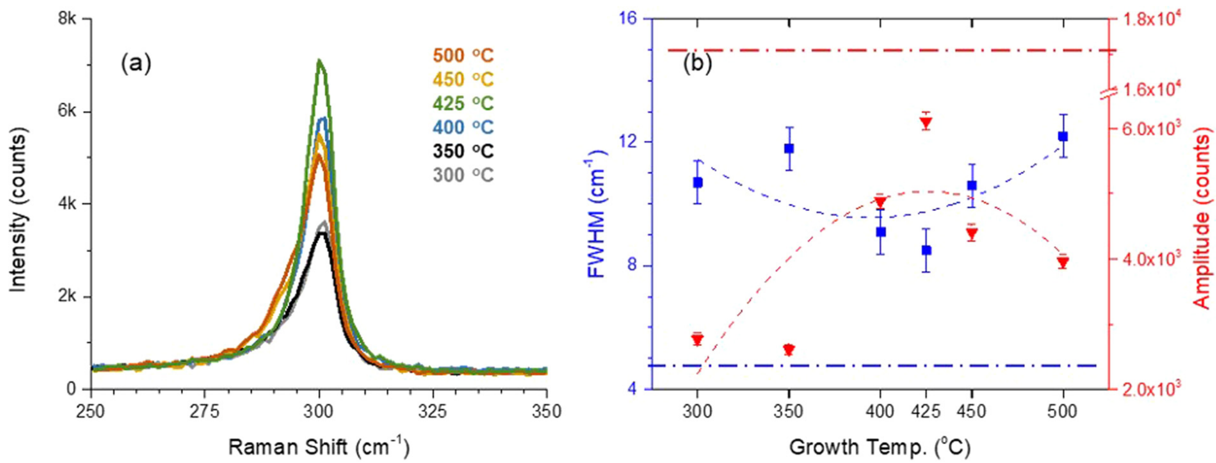

FIG. 2. (a) Raman spectra of Ge/mica films grown at increasing temperatures from 300 to 500 °C. (b) Quantitative parameters extracted from Gaussian fits of peaks in (a). Blue and red horizontal long-short-dashed lines indicate FWHM and amplitude values for single crystal Ge wafer. Curved dashed lines are included to guide the eye.

mica(006). From this, the mica *c*-axis is calculated to be 19.96 Å, in reasonable agreement with XRD database values. In addition, the scans of films grown at 400 °C and 425 °C exhibit a second peak at about $2\theta = 27.27°$. This peak sits on the shoulder of strong mica intensity and is due to Ge(111), indicating crystalline film content. The peak's location gives a lattice constant of 5.659 Å, in good agreement with a(Ge) = 5.658 Å. As indicated in Fig. 3(a), no other film peaks were exhibited in the scans of any films, indicating single orientation growth along [111]. In good agreement with Raman spectroscopy data, XRD $\theta/2\theta$ scans indicate 425 °C to be the optimal growth temperature to achieve crystallinity in the Ge film.

A single XRD scan covers a very limited region of reciprocal space. To further investigate the out-of-plane dispersion and gain more information regarding film quality,[32] a high resolution XRD reciprocal space map (HRXRD RSM) of the mica(006) and Ge(111) peaks was collected for the optimal film grown at 425 °C. A simulation of the Ge/mica heterostructure's reciprocal space is shown in Fig. 4(a), with the scanned region as inset. Figure 4(b) shows the experimental data. The x and z axes labels in black are in terms of the mica Miller indices h and l, while the numbers in red are reciprocal space vectors Q_x and Q_z in units of Å^{-1}. It is clear from the RSM that the Ge film exhibits a high level of out-of-plane order following from that of the mica substrate. The location of the Ge(111) peak at precisely the theoretical position given its atomic structure shows that the Ge film is completely relaxed. Cuts of the RSM along the $\theta/2\theta$ and rocking curve (RC) scanning directions are indicated with dashed lines and included in Figs. 4(c)–4(e). From the $\theta/2\theta$ scan in Fig. 4(c), the extracted Ge(111) location and FWHM are $27.277° \pm 0.001°$ and $0.154° \pm 0.003°$, respectively. With this information, a lower limit to the vertical

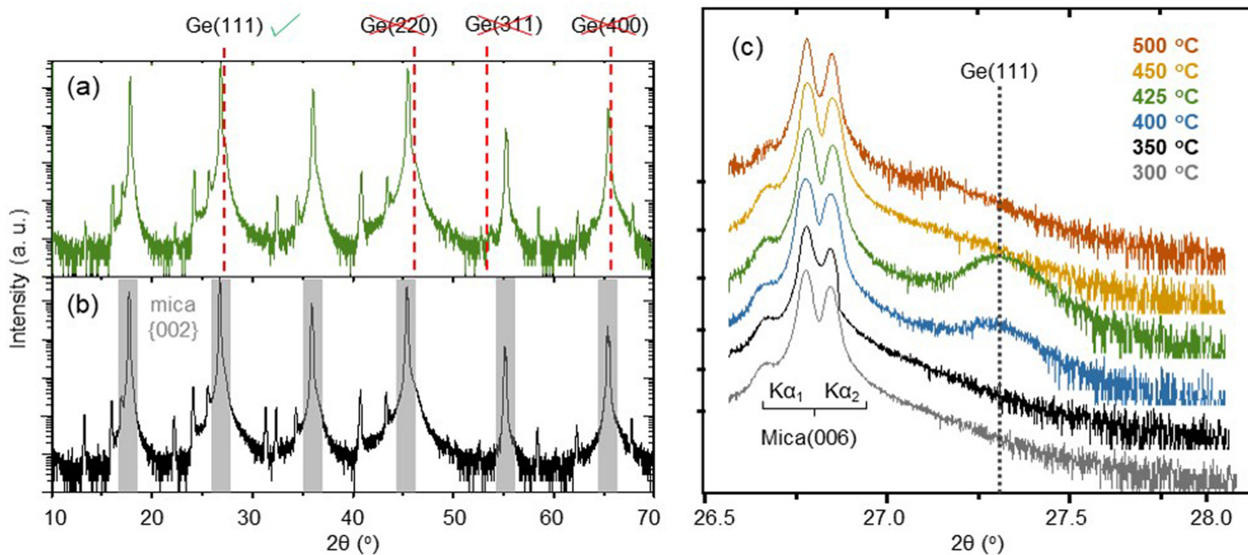

FIG. 3. Wide range X-ray diffraction $\theta/2\theta$ scan of (a) Ge film on mica grown at 425 °C, and (b) bare mica(001) for reference. Of the (111), (220), (311), and (400) peaks indicated by vertical dashed lines, only the Ge(111) peak at $2\theta = 27.27°$ can be identified. (c) Narrow range XRD $\theta/2\theta$ scans of Ge/mica films grown at increasing temperatures from 300 to 500 °C. Theoretical Ge(111) peak location is indicated by a vertical dashed line. Ge(111) peak appears in a narrow temperature window of 400–425 °C.

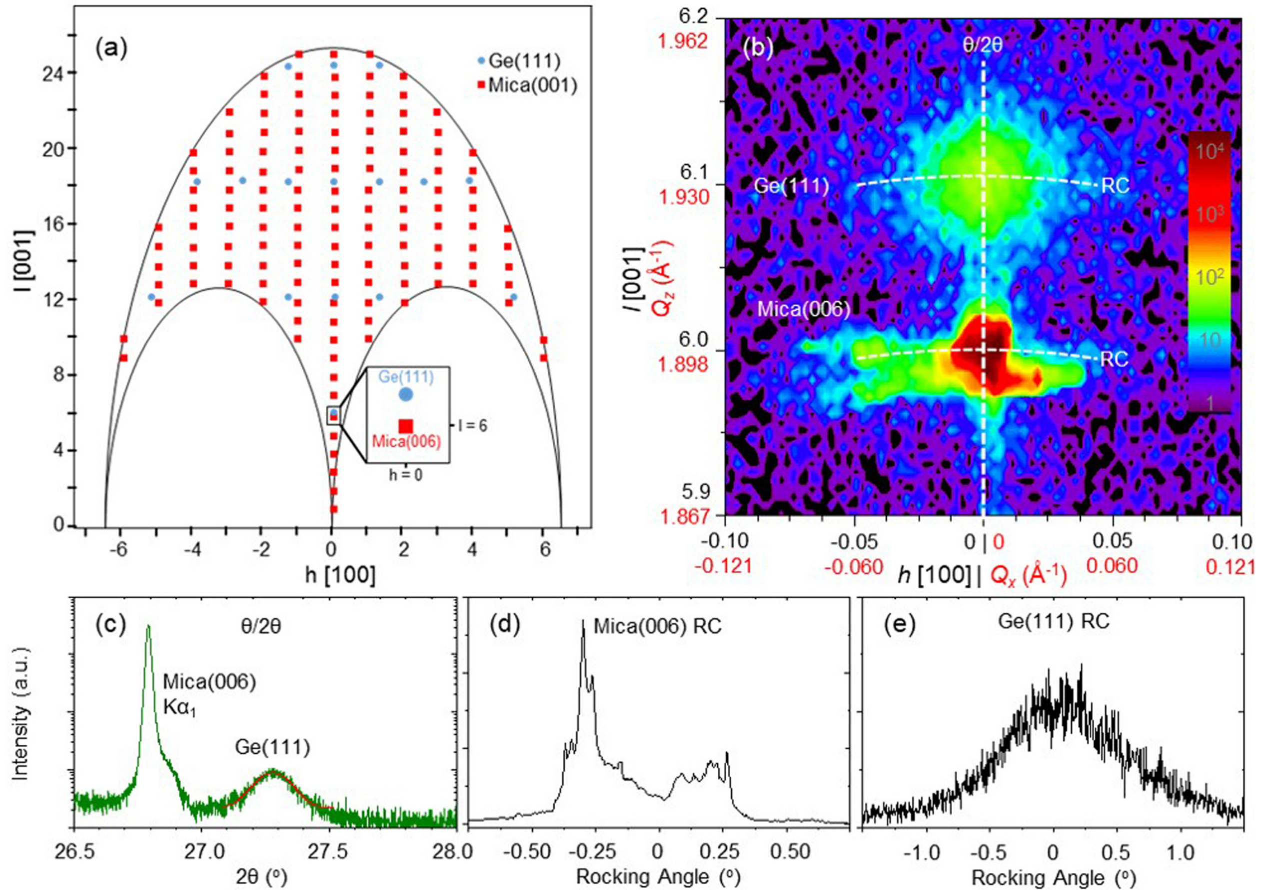

FIG. 4. (a) Schematic of reciprocal space of Ge(111) film on the mica(001) substrate. Miller indices h [100] and l [001] are with respect to the mica substrate. Blue circles and red squares represent diffraction spots due to the film and substrate, respectively. The inset shows the scanned region of reciprocal space including the Ge(111) and mica(006) peaks. (b) High resolution XRD reciprocal space map (RSM) of Ge/mica film grown at 425 °C. The black numbers are the x and z axes in terms of the mica Miller indices h and l, while the red numbers are in terms of Q_x and Q_z (Å^{-1}). Note that the reciprocal spot mica(006) is located at h = 0 and l = 6. (c) HRXRD $\theta/2\theta$ scan, (d) mica(006) rocking curve, and (e) Ge(111) rocking curve.

coherent domain size of approximately 61 nm is estimated using the Scherrer equation[33]

$$D \approx \frac{\lambda}{\beta_D \cos\theta}. \quad (3)$$

Here the diameter D of the coherent domain sizes in the direction parallel to the momentum transfer vector (out-of-plane) is estimated given the X-ray wavelength (λ), the broadening of a crystalline peak quantified by FWHM after Gaussian deconvolution with an appropriate instrument response function (β_D), and half the 2θ location of the crystalline peak (θ). Taking the FWHM of the mica (006) peak of approximately 0.017° to be the instrument response function, the estimation of approximately 61 nm is on the order of the film thickness, indicating that the crystalline grains extend near the entire thickness of the film.

The mica(006) rocking curve shown in Fig. 4(d) exhibits a non-Gaussian intensity profile with an angular dispersion of about 0.7°. This was seen for all mica substrates and may be due to imperfect cleaving of the substrate prior to film growth, the substrate's flexibility, or sample mounting. Figure 4(e) shows the Ge(111) rocking curve. It exhibits a Gaussian profile with an FWHM of 1.11° ± 0.02°, indicating that the (111) surface planes of Ge do not deviate far from the mica's (001) orientation. This level of out-of-plane dispersion is indicative of a highly ordered but imperfect crystalline film. The scans confirm that the out-of-plane epitaxial relation is Ge[111]||mica[001].

3. XRD pole figure analysis and in-plane epitaxy

a. Mica(001) substrate. To determine the in-plane epitaxy between Ge and mica, XRD pole figures were taken at film and substrate peaks of the Ge/mica film grown at 425 °C. Figure 5(a) shows the mica{111} XRD pole figure, which was collected by setting $2\theta = 20.49°$ ($d_{111} = 4.332$ Å). The data exhibit four asymmetric mica poles: the (111), $(1\bar{1}1)$ poles are located at $\chi = 72.7°$ (∼72° experimentally) and separated 59.4° in ϕ; the (021) and $(0\bar{2}1)$ poles are located at $\chi = 77.2°$ (∼78° experimentally) and separated 180° in ϕ. It is worth noting that the {021} poles occur at $2\theta = 19.86°$ ($d_{111} = 4.468$ Å) and were picked up by the XRD detector due to the wide slits used to maximize signal strength. The average FWHMs of the mica {111} and mica {021} poles along the azimuthal and polar directions are 1.0° ± 0.5° and 5.1° ± 0.5°, respectively. From the location of the poles, the orientation of the mica unit axes [100] and [010] can be determined and is indicated on Fig. 5(a).

b. Ge(111) film. Without adjusting the sample position after the measurement of the mica pole figure, the Ge{111}

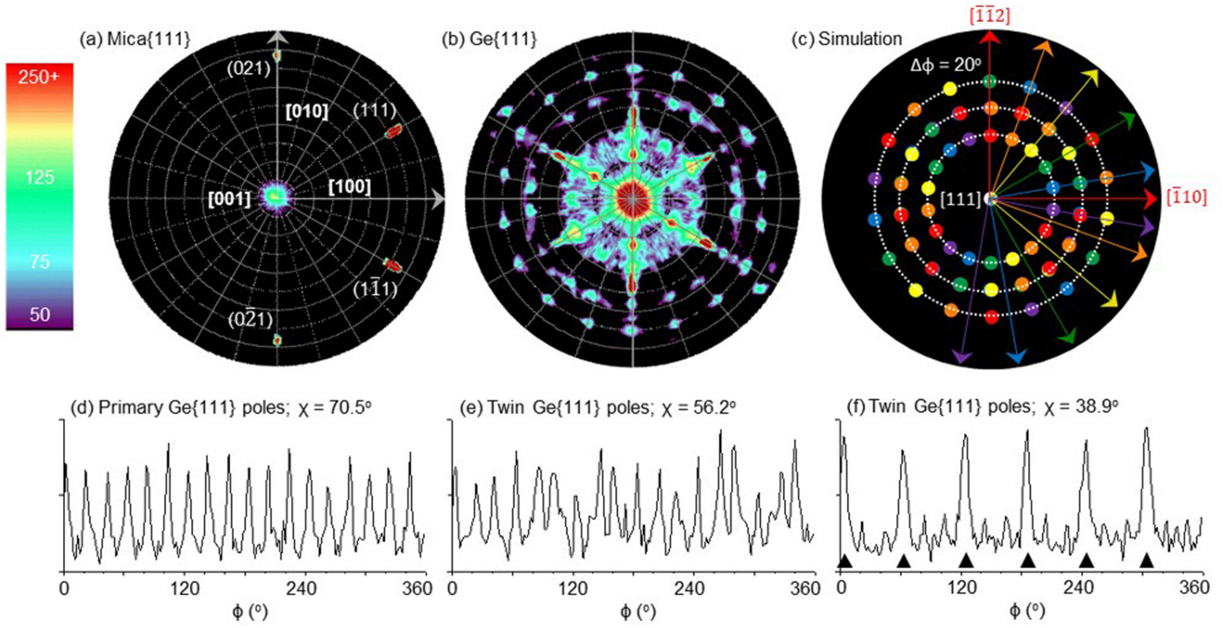

FIG. 5. (a) Mica{111} and (b) Ge{111} X-ray diffraction pole figures of Ge film grown on mica at 425 °C. (c) Simulation indicating the positions of poles from each rotational domain and corresponding unit axes orientations. Azimuthal φ scans of primary and twin Ge{111} poles at (d) $\chi = 70.5°$, (e) $\chi = 56.2°$, (f) $\chi = 38.9°$. Markers in (f) indicate overlapping mica substrate signal.

pole figure was collected by setting $2\theta = 27.28°$ ($d_{111} = 3.267$ Å) and is shown in Fig. 5(b). The ring of eighteen discrete poles at $\chi \sim 70°$ is the primary {111} poles of [111] oriented Ge. Single crystal Ge with one rotational domain should exhibit just three of these peripheral poles spaced equally azimuthally ($\Delta\phi = 120°$); thus we can attribute the large number of poles to six independent rotational domains ($6 = 18/3$, $\Delta\phi = 20°$). Additional rings of eighteen poles are also seen at $\chi \sim 56°$ and $\chi \sim 38°$, which originate from crystal twinning about various {111} directions. Azimuthal ϕ scans of each ring are included in Figs. 5(d)–5(f). In agreement with the Ge{111} pole figure, each shows 18 discrete poles with an average separation between adjacent poles of $\Delta\phi = 20 \pm 2°$. ϕ scans of the primary and twin Ge{111} poles in Figs. 5(d) and 5(e) contain poles with a near equal intensity, which implies equal population of each rotational domain. Six of the eighteen poles in Fig. 5(f) are of greater intensity due to overlapping with signal from the substrate. A simulation indicating six rotational domains with twinning is shown in Fig. 5(c). The theoretical location of each pole agrees well with the experimental data. Unit axes directions are color-coded to match the poles of the corresponding rotational domain. All additional signal not included in the simulation is due to further twinning of the twinned domains (twins of twins) and background from the mica substrate. These are indicated in Fig. S2 (supplementary material).

4. Epitaxial relationship between Ge and mica

From the information provided by the mica{111} and Ge{111} XRD pole figures, one can determine the in-plane epitaxial relationship between the film and the substrate. Because there are six rotational domains present in the Ge film, there exist six in-plane epitaxial relationships between Ge and mica. Defining ϕ_{off} as the angle between Ge[$\bar{1}$10] and mica[100], we can simultaneously express each: $\phi_{off} = (20n)°$, where $n = 0$, 1, 2, 3, 4, and 5. These results reveal that a crystalline Ge film can be epitaxially grown on a mica substrate despite the large 23% interface lattice mismatch between Ge(111) and mica(001): $(a_{Ge} - a_{mica})/a_{mica} = (4.0–5.2)/5.2 = -0.23$.

C. Superlattice area mismatch model

A geometrical superlattice area mismatch model was applied to the Ge/mica heterostructure interface to shed some light on the observed heteroepitaxy.[34–36] Minimization of superlattice area and area mismatch was calculated for each of the possible epitaxial alignments of the hexagonal Ge(111) unit mesh on the pseudo-hexagonal K-terminated unit mesh of mica(001). The simulation requires only the geometry of each unit mesh at the interface [shown for Ge and mica in Figs. 6(b) and 6(c), respectively]: nearest-neighbor distances a_{Ge}, b_{Ge}, a_{mica}, b_{mica}, and the unit mesh angles α_{Ge}, and α_{mica} for the Ge(111) and mica(001) surfaces. The corresponding in-plane distances are 4.000 Å, 4.000 Å, 5.189 Å, 5.192 Å, 60°, and 60.02°. The use of a pseudo-hexagonal lattice for the surface of mica(001) is supported experimentally by the observed hexagonal symmetry in low energy electron diffraction (LEED) patterns.[19,26,37,38] Superlattice area, A, is defined as the area in which a coincident lattice occurs between the overlayer and the substrate. Superlattice area mismatch, ΔA, is defined as the area over which the film and substrate superlattices do not overlap, and is given by

$$\Delta A = A\left[\left(\frac{\Delta u}{u}\right) + \left(\frac{\Delta v}{v}\right) + \Delta\alpha\cot\alpha\right], \tag{4}$$

where u and v are the superlattice lengths separated by angle α, and Δu, Δv, and $\Delta\alpha$ are the differences in each parameter

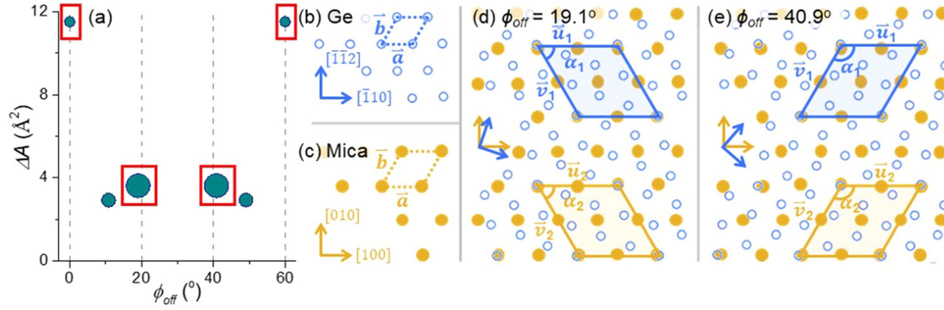

FIG. 6. Superlattice area mismatch simulation showing the three most likely results for Ge(111) on mica(001). (a) Bubble plot of mismatch area ΔA *vs* ϕ_{off}. Bubble diameter is inversely proportional to superlattice area A (i.e., larger bubble implies greater likelihood of observation). Experimentally observed rotational domains are emphasized with red boxes. (b) Ge(111) unit mesh shown as open blue circles. (c) Mica(001) unit mesh shown as filled gold circles. 2D superlattice overlays of Ge(111) on mica(001) for (d) $\phi_{\rm off} = 19.1°$ and (e) $\phi_{\rm off} = 40.9°$ representing the two most favorable configurations predicted by the model. The rotation angle $\phi_{\rm off}$ is defined as the angle between Ge [$\bar{1}$10] and mica [100] directions.

between the overlayer and the substrate. Superlattice area mismatch (ΔA) is directly proportional to superlattice area (A); thus, small superlattice areas in addition to small mismatches between the superlattice lengths and angles of the film and substrate are favorable. The maximum area limit of each superlattice was set to 250 Å^2, and the maximum allowable mismatch between the superlattice lengths and superlattice angles was limited to <6%. The calculated results are listed in Table II and plotted in Fig. 6(a).

These results are illustrated in a bubble plot of ΔA *vs.* ϕ_{off} in Fig. 6(a), where the bubble diameter is inversely proportional to A (i.e., larger bubble implies greater likelihood of observation). Of the three most likely sets of results, two are consistent with the observed epitaxy [$\phi_{off} = 19.1°$, 40.9°, 0°, and 60°, emphasized in Fig. 6(a) with red boxes]. The set of most likely results at $\phi_{off} = 19.1°$ and 40.9° is illustrated schematically in Figs. 6(d) and 6(e) to show examples of superlattice formation. Because of the 60° periodicity of the Ge(111) unit mesh, this set of results is equivalent to $\phi_{off} = 79.1°$ and 100.9°; the geometrical model is also able to explain the domains at rotations of ~80° and 100°. Thus, each of the six experimentally observed rotational domains at $\phi_{off} = (20n)°$, $n = 0, 1,\ldots, 5$ arises from superlattice area mismatch calculations.

It is quite remarkable that the simple superlattice area mismatch model can qualitatively predict the observed main six orientation domains in the Ge film. However, there are other orientations, one set of which (at 10.9° and 49.1°) (bubbles without red boxes) has both a lower A and a lower ΔA than the set at 0° and 60°, which are predicted by the model that does not match the experimental data. These discrepancies are probably due to the complicated nature of the mica substrate such as surface termination,[19,37–40] steps,[20] and contaminations,[19] which will all affect the Ge epitaxy.

D. Reflection high energy electron diffraction

It is often the case that the crystalline quality of a bulk film differs from that of the film surface. Surface-sensitive RHEED was collected to investigate the surface crystal structure for comparison to data for the bulk. Figure 7(a) is an experimental RHEED pattern collected at an arbitrary azimuthal angle from the Ge/mica film grown at 425 °C. Clear diffraction spots are observed in addition to several faint rings. Patterns at all azimuthal angles look similar. The uniform ring structure is a result of diffraction from polycrystalline content on the film surface. The spots originate either from crystalline grains exhibiting a fiber texture in which there is no preferred in-plane orientation, or from epitaxial grains in which a preferred in-plane orientation exists. One can differentiate these two possibilities by measuring the intensity distribution of the spots as a function of azimuthal angle. If the intensity of the spots is uniform as a function of the azimuthal angle, the film exhibits a fiber texture; if the intensity is azimuthally dependent, some portion of the grains are epitaxially grown on the substrate. In the current experiment, we are unable to obtain reliable intensity as a function of the azimuthal angle because some patterns from different azimuthal angles were distorted due to charging of the mica substrate. Therefore, we cannot conclude from these patterns that there exists a preferred in-plane orientation. However, since qualitatively the spots appear at all

TABLE II. Relative likelihood of geometrical superlattice area matching results for Ge(111) on mica(001), ranked 1 (most likely) to 3 (least likely) within the given constraints.

Relative Likelihood	$\phi_{\rm off}$ (°)	u (Å) Ge | Mica	v (Å) Ge | Mica	α (°) Ge | Mica	A (Å^2) Ge | Mica	$\Delta A/A$ (%)
1	19.1	10.58 | 10.38	10.58 | 10.38	60.00 | 60.02	96.99 | 93.35	3.91
	40.9	10.58 | 10.38	10.58 | 10.38	120.00 | 119.98	96.99 | 93.35	3.91
2	10.9	13.86 | 13.74	24.00 | 23.80	30.00 | 29.98	166.28 | 163.36	1.78
	49.1	13.86 | 13.74	24.00 | 23.80	150.00 | 150.02	166.28 | 163.36	1.78
3	0.0	27.71 | 26.98	16.00 | 15.58	30.00 | 29.98	221.70 | 210.03	5.48
	60.0	27.71 | 26.98	16.00 | 15.58	150.00 | 150.02	221.70 | 210.03	5.48

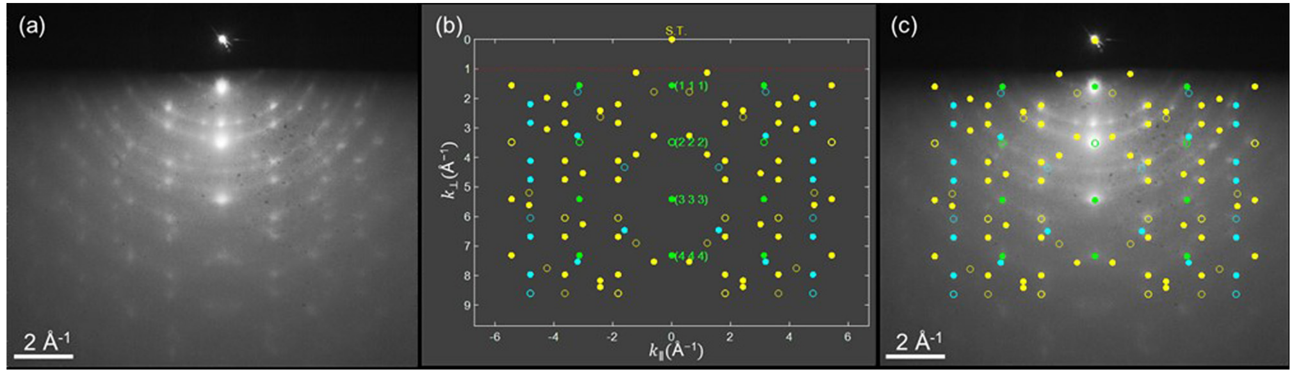

FIG. 7. (a) Experimental RHEED pattern of Ge(111) film grown on mica at 425 °C. The electron was incident at an arbitrary azimuthal angle on the Ge film with 20 keV energy. The scale bar is 2 Å^{-1}. (b) Simulated RHEED pattern from Ge crystal or crystalline film. This pattern consists of a straight through spot (labeled as "S.T."), a shadowing edge (red dashed line), and the diffraction spots from three zone axes [$10\bar{1}$] (yellow), [$3\bar{1}\bar{2}$] (blue), and [$2\bar{1}\bar{1}$] (green). The Miller indices of the central spots ($k_{||} = 0$) are labeled and indicate (111) out-of-plane orientation. The single diffraction spots are denoted by filled circles, while the double diffraction spots are denoted by open circles. A +200 V surface potential relative to the vacuum level from the charging effect of mica was included in the simulation. The coordinate system centers at the straight through spot. The horizontal and vertical axes are the momentum transfer parallel ($k_{||}$) and perpendicular ($k_\perp$) to the sample surface, respectively. Momentum transfer is in units Å^{-1}. (c) Simulated diffraction spots overlaid on the experimental RHEED pattern using the same scale, showing one-to-one correspondence.

azimuthal angles, we conclude that there should be a strong fiber texture component in the near-surface region of the film. Also, the fact that the pattern is symmetric about the center vertical axis implies that there exists crystal twinning, which readily occurs in crystals having the diamond structure.[41]

Quantitative analysis of the fiber component of the film from the RHEED pattern was carried out with the aid of computer simulation using MATLAB. Details about the simulation are presented in the Supplementary Information. Figure 7(b) shows the simulated RHEED pattern generated under the following assumptions: (1) the near-surface region of the Ge film has (111) out-of-plane orientation (supported by XRD of the bulk film); (2) the near-surface region of the Ge film has a fiber texture component; (3) twin crystals form about the {111} family of planes of Ge; (4) double-diffraction occurs in the Ge film, which gives rise to the emergence of kinematically forbidden reflections[42,43] such as (222); and (5) a positive potential, U relative to the vacuum level accumulated on the sample surface under electron illumination due to the charging effect of mica.[44]

Several features are combined and shown in Fig. 7(b). The Miller indices of the central spots ($k_{||} = 0$) are labeled, revealing (111) out-of-plane orientation. The Miller indices of the remaining spots that are not due to crystal twinning can be found in Fig. S5 (supplementary material). Spots in different colors correspond to diffraction patterns as viewed from different zone axes: yellow for [$10\bar{1}$], blue for [$3\bar{1}\bar{2}$], and green for [$2\bar{1}\bar{1}$]. Spots from different zone axes show up simultaneously because of the crystalline content exhibiting a fiber texture. The geometrical relationship between these three axes in the reciprocal space of Ge is shown in Fig. S3 (supplementary material). Single-diffraction and double-diffraction spots are denoted by filled circles and open circles, respectively. A decomposition of Fig. 7(b) into the individual contributions from crystal twinning, fiber texture, and double diffraction is shown in Fig. S4 (supplementary material). It is also worth pointing out that Fig. 7(b) is generated after the surface potential correction. Both the uncorrected (using the same notation as previously described) and the corrected (denoted by red stars) patterns are overlaid on the experimental RHEED pattern in Fig. S5 (supplementary material), sharing the straight-through spot. By fitting the positions of the simulated diffraction spots to the experimental results, we found the surface potential $U \approx +200$ V. All spots are shifted toward the shadowing edge (denoted by the red dashed line) after this surface potential correction.

In Fig. 7(c), the simulated spots from Fig. 7(b) are superimposed on the experimental RHEED pattern in Fig. 7(a) using the same scale. The one-to-one correspondence between the simulation and the experiment confirms our previous assumptions. Comparing results from XRD pole figure and RHEED patterns, both show the existence of twins in the Ge film about the {111} planes. However, the RHEED patterns indicate a fiber texture near the film surface, whereas XRD shows six orientation domains in the bulk of film. A word of caution, the RHEED study was performed *ex situ*; any contamination or oxidation of the film will affect the near surface structure and be detected by surface-sensitive RHEED. Sequential *in situ* depositions should be utilized to achieve optimal interface quality when growing films on Ge/mica.

E. Hall mobility of Ge film on mica

Room temperature Hall effect measurements were conducted to investigate the correlation between the Ge films' electrical properties and growth temperature. Each film was determined to be p-type. The hole mobility μ_h, resistivity ρ, and carrier concentration n are listed in Table III.

In addition to exhibiting the optimal crystalline quality, Hall effect data suggest that the 425 °C sample also exhibits enhanced electrical properties. Its hole mobility of 46.1 ± 5.6 cm^2/V s is much higher than mobilities for all other samples. It also exhibits the highest charge carrier concentration ($36.9 \pm 4.7 \times 10^{17}$ cm^{-3}) and the lowest resistivity (0.037 ± 0.002 Ω cm). Electrical properties tend to degrade upon deviating from this growth temperature, with the

TABLE III. Room temperature Hall effect measurements of Ge films grown at various temperatures. Electrical properties measured include charge carrier type, Hall mobility (μ_h), resistivity (ρ), and charge carrier concentration n ($= N_A - N_D$, where N_A and N_D are acceptor and donor concentrations, respectively).

Growth Temp. (°C)	Type	μ_h (cm^2/V s)	ρ (Ω cm)	$n = N_A - N_D$ ($\times 10^{17}$ cm^{-3})
300	p	7.8 ± 2.3	12.0 ± 0.6	0.7 ± 0.2
350	p	13.9 ± 0.5	0.45 ± 0.02	10.1 ± 0.4
400	p	11.9 ± 2.5	0.21 ± 0.01	25.7 ± 5.6
425	p	46.1 ± 5.6	0.037 ± 0.002	36.9 ± 4.7
450	p	10.0 ± 0.4	0.23 ± 0.01	26.6 ± 1.0
500	p	5.9 ± 0.9	2.4 ± 0.1	4.5 ± 0.7

exception of the film grown at 350 °C, which exhibits a slightly higher mobility than the 400 °C film. This may be due to damage to the 400 °C film incurred between the time it was grown and the time it was tested, or from a problem with one or more of the indium contacts. Resistivity in the 300 °C sample is quite high compared to others, likely due to surface scratches incurred during sample preparation.

It should be noted that overall these mobilities are lower than the bulk single crystal Ge (~1800 cm^2/V s)[45] and on the low end as compared to other germanium films grown at similar temperatures. Hall mobility depends on a multitude of factors such as growth conditions, growth rate, thickness, and substrate, which then determine grain size, carrier type, film quality, and impurity concentration. Examples include: approx. 150 nm thick Ge films epitaxially grown on single crystal CaF_2(111) at 550–575 °C exhibit mobilities in the range of 50–150 cm^2/V s and hole concentrations of 6×10^{17}–10^{18}/cm^3;[46] micron-thick single crystal Ge film grown on Si(100) at 440 °C exhibits a mobility of 1040 cm^2/V s with a hole concentration of 1.6×10^{16} cm^{-3};[47] a mobility of 107 cm^2/V s was measured for 400 nm thick Ge deposited on quartz at 825 °C;[48] and the mobilities of ~500 nm thick $Ge_{0.95}Sn_{0.05}$ alloy films grown on CaF_2(111) and CaF_2(100) at 400 °C are ~90 and 100 cm^2/V s, respectively.[23] As the Ge/mica films studied herein are quite thin (less than 100 nm), it is likely that the lateral grain size is limited, which would impact charge carrier transport due to scattering at grain boundaries. By increasing the film thickness while keeping all else constant, one would expect to observe an increase in mobility.

F. Discussion

Degradation of crystalline quality in Ge films grown above 425 °C is likely due to temperature-induced changes to the muscovite mica surface. Previous studies have observed changes in optical absorption spectra of muscovite upon heat treatment at 500 °C and attributed these changes to the formation of a defect structure.[49] Structural degradation may begin on the mica surface at temperatures just below this, thus producing an imperfect surface for Ge nucleation. In addition, desorption of surface potassium atoms at elevated temperature[39] causes further changes in the surface structure and may even induce chemical reactions between mica and germanium. While below the threshold (experimentally determined to be 425 °C) increasing the substrate temperature improves Ge film crystallinity through enhanced adatom kinetic energy and diffusion, above it the increasingly disordered mica surface becomes detrimental to film quality.

The optimal Ge/mica growth temperature is not too far from that needed for the chemical epitaxy of Ge on other single crystal substrates. Examples include: Ge on cleaved (100) faces of NaCl, NaF, and MgO at temperatures around 500 °C, on CaF_2(111) at temperatures between 450 and 700 °C depending on the deposition rate,[50] and on CaF_2(100)/sapphire at temperatures between 250 and 550 °C.[51] Our prior work has demonstrated that nearly single crystal Ge film with large grains can be grown on CaF_2(100) buffered cube textured Ni(100) foil at 400 °C and avoid the formation of germanide,[52] Ge film on oblique-angle-deposited biaxial CaF_2(111)$\langle 121 \rangle$/glass at ~400 °C,[53] and oblique-angle-deposited biaxial Ge(001)$\langle 110 \rangle$ on amorphous SiO_2/Si(001) at ~375 °C.[54] Note the incident flux in the oblique angle deposition makes an oblique angle with respect to the surface normal and can enhance lateral adatom diffusions to form biaxial films.[55] In addition to oblique angle deposition, the crystallization temperature can also be lowered if a surfactant such as Sn or Sb is used in the deposition of Ge. For example, one can predeposit Sn before Ge deposition to form $Ge_{1-x}Sn_x$ film on CaF_2(100) and CaF_2(111) above 250 °C,[23] or deposit one monolayer Sb on top of amorphous Ge deposited on Si(100) and anneal at around 400 °C.[21]

IV. CONCLUSION

In contrast to literature reports, which have indicated that elemental semiconductors cannot be epitaxially grown on mica through van der Waals epitaxy at any elevated temperature, we have achieved the epitaxial growth of Ge(111) film on a mica substrate at a temperature around 425 °C. Furthermore, Raman spectroscopy, X-ray diffraction, and Hall effect measurements have indicated a clear dependence of crystalline and electrical properties on growth temperature, each degrading upon deviation from the optimal temperature. Detailed X-ray pole figure analysis revealed the existence of multiple rotational domains in the epitaxial film with the angle between Ge[$\bar{1}$10] and mica[100] of the dominant domains equal to $\phi_{off} = (20n)^{\circ}$, where $n = 0, 1, 2, 3, 4, 5$. These domains are qualitatively accounted for based on a superlattice area mismatch model. The surface of the Ge film was characterized by RHEED, which indicated the existence of a fiber texture component in the near-surface region. This likely forms due to post-deposition atmospheric exposure; thus when using Ge/mica as a substrate, *in situ* deposition of the film layer is essential to obtain the optimal interface. Our

observation of Ge epitaxy through van der Waals forces paves the way toward the possibility of growing single crystal semiconductor films by vdWE without the constraints imposed by lattice and symmetry matching with the substrate.

SUPPLEMENTARY MATERIAL

See supplementary material for Raman spectroscopy of single crystal Ge, additional analysis of the poles observed in the Ge{111} XRD pole figure, and additional discussion of RHEED results.

ACKNOWLEDGMENTS

This work is supported by the New York State Foundation of Science, Technology and Innovation (NYSTAR) through Focus Center-New York C130117, the National Science Foundation Award DMR-1305293, NSF REU DMR-1560266, and Rensselaer. We thank I. Bhat, D. Mohanty, and B. Colwill for their assistance with Hall measurements.

[1]J. Werner, M. Oehme, M. Schmid, M. Kaschel, A. Schirmer, E. Kasper, and J. Schulze, Appl. Phys. Lett. **98**(6), 061108 (2011).
[2]L. Tang, S. E. Kocabas, S. Latif, A. K. Okyay, D. S. Ly-Gagnon, K. C. Saraswat, and D. A. B. Miller, Nat. Photonics **2**(4), 226–229 (2008).
[3]L. Colace, G. Masini, G. Assanto, H. C. Luan, K. Wada, and L. C. Kimerling, Appl. Phys. Lett. **76**(10), 1231–1233 (2000).
[4]R. M. Fletcher, D. K. Wagner, and J. M. Ballantyne, Appl. Phys. Lett. **44**, 967–969 (1984).
[5]R. N. Ghosh, B. Griffing, and J. M. Ballantyne, Appl. Phys. Lett. **48**(5), 370–371 (1986).
[6]M. A. Green, K. Emery, Y. Hishikawa, W. Warta, and E. D. Dunlop, Prog. Photovoltaics **24**(7), 905–913 (2016).
[7]C. Algora, E. Ortiz, I. Rey-Stolle, V. Diaz, R. Pena, V. M. Andreev, V. P. Khvostikov, and V. D. Rumyantsev, IEEE Trans. Electron Devices **48**(5), 840–844 (2001).
[8]M. A. Green, Adv. Mater. **13**(12–13), 1019–1022 (2001).
[9]C. A. Dimitriadis, Solid State Commun. **56**(11), 925–927 (1985).
[10]W. Seifert, G. Morgenstern, and M. Kittler, Semicond. Sci. Technol. **8**(9), 1687–1691 (1993).
[11]L. Carnel, I. Gordon, D. Van Gestel, G. Beaucarne, and J. Poortmans, J. Appl. Phys. **100**(6), 063702 (2006).
[12]C. A. Dimitriadis, J. Phys. D: Appl. Phys. **18**(12), 2489–2495 (1985).
[13]A. Koma, Thin Solid Films **216**(1), 72–76 (1992).
[14]M. I. B. Utama, Q. Zhang, J. Zhang, Y. Yuan, F. J. Belarre, J. Arbiol, and Q. Xiong, Nanoscale **5**(9), 3570–3588 (2013).
[15]D. Mohanty, W. Xie, Y. Wang, Z. Lu, J. Shi, S. Zhang, G.-C. Wang, T.-M. Lu, and I. B. Bhat, Appl. Phys. Lett. **109**(14), 143109 (2016).
[16]F. S. Ohuchi, B. A. Parkinson, K. Ueno, and A. Koma, J. Appl. Phys. **68**(5), 2168–2175 (1990).
[17]K. Ueno, K. Saiki, T. Shimada, and A. Koma, J. Vac. Sci. Technol. A **8**(1), 68–72 (1990).
[18]Y. B. Yang, L. Seewald, D. Mohanty, Y. Wang, L. H. Zhang, K. Kisslinger, W. Xie, J. Shi, I. Bhat, S. Zhang, T.-M. Lu, and G.-C. Wang, Appl. Surf. Sci. **413**, 219–232 (2017).
[19]H. Poppa and A. G. Elliot, Surf. Sci. **24**(1), 149–163 (1971).
[20]W. de Poel, S. Pintea, J. Drnec, F. Carla, R. Felici, P. Mulder, J. A. A. W. Elemans, W. J. P. van Enckevort, A. E. Rowan, and E. Vlieg, Surf. Sci. **619**, 19–24 (2014).
[21]H. J. Osten, J. Klatt, and G. Lippert, Appl. Phys. Lett. **60**(1), 44–46 (1992).
[22]Q. Wang, K. Xu, Z. Wang, F. Wang, Y. Huang, M. Safdar, X. Zhan, F. Wang, Z. Cheng, and J. He, Nano Lett. **15**, 1183–1189 (2015).
[23]A. J. Littlejohn, T.-M. Lu, L. H. Zhang, K. Kisslinger, and G.-C. Wang, CrystEngComm **18**, 2757–2769 (2016).
[24]J. K. Dash, L. Chen, T.-M. Lu, G.-C. Wang, L. H. Zhang, and K. Kisslinger, CrystEngComm **16**, 8794–8804 (2014).
[25]L. Chen, J. K. Dash, P. Su, C. F. Lin, I. Bhat, T.-M. Lu, and G.-C. Wang, Appl. Surf. Sci. **288**, 458–465 (2014).
[26]D. Winau, R. Koch, A. Fuhmann, and K. H. Rieder, J. Appl. Phys. **70**(6), 3081–3087 (1991).
[27]Y.-P. Zhao, G.-C. Wang, and T.-M. Lu, *Characterization of Amorphous and Crystalline Rough Surfaces: Principles and Applications* (Academic Press, San Diego, 2000).
[28]K. A. Bratland, Y. L. Foo, T. Spila, H.-S. Seo, R. T. Haasch, D. Desjardins, and J. E. Greene, J. Appl. Phys. **97**(4), 044904 (2005).
[29]S. Vadavalli, S. Valligatla, B. Neelamraju, M. H. Dar, A. Chiasera, M. Ferrari, and N. R. Desai, Front. Phys. **2**(57), 1–9 (2014).
[30]P. Dutta, M. Rathi, Y. Yao, Y. Gao, G. Majkic, M. Iliev, J. Martinez, B. Holzapfel, and V. Selvamanickam, RSC Adv. **4**(40), 21042–21048 (2014).
[31]J. Fortner, R. Q. Yu, and J. S. Lannin, Phys. Rev. B **42**(12), 7610–7613 (1990).
[32]P. F. Fewster, Crit. Rev. Solid State Mater. Sci. **22**(2), 69–110 (1997).
[33]G. K. Williamson and R. E. Smallman, Philos. Mag. **1**(1), 34–46 (1956).
[34]A. Zur and T. C. McGill, J. Appl. Phys. **55**(2), 378–386 (1984).
[35]A. S. Yapsir, C. H. Choi, and T.-M. Lu, J. Appl. Phys. **67**(2), 796–799 (1990).
[36]X. Sun, Z. Lu, W. Xie, Y. Wang, J. Shi, S. Zhang, M. A. Washington, and T.-M. Lu, Appl. Phys. Lett. **110**(15), 153104 (2017).
[37]F. Ostendorf, C. Schmitz, S. Hirth, A. Kuhnle, J. J. Kolodziej, and M. Reichling, Nanotechnology **19**, 305705 (2008).
[38]K. Muller and C. C. Chang, Surf. Sci. **14**, 39–51 (1969).
[39]B. Putsche, L. Tumbek, and A. Winkler, J. Chem. Phys. **137**(13), 134701 (2012).
[40]P. A. Campbell, L. J. Sinnamon, C. E. Thompson, and D. G. Walmsley, Surf. Sci. **410**(2), L768–L772 (1998).
[41]E. Billig and M. S. Ridout, Nature **173**(4402), 496–497 (1954).
[42]J. B. Roberto, B. W. Batterman, and D. T. Keating, Phys. Rev. B **9**(6), 2590–2599 (1974).
[43]A. Ichimiya and P. I. Cohen, *Reflection High-Energy Electron Diffraction* (Cambridge University Press, Cambridge, 2004).
[44]J. Cazaux, J. Electron Spectrosc. Relat. Phenom. **176**(1–3), 58–79 (2010).
[45]D. M. Brown and R. Bray, Phys. Rev. **127**(5), 1593–1602 (1962).
[46]A. L. Pundsack, J. Appl. Phys. **34**(8), 2306–2308 (1963).
[47]Y. Ohmachi, T. Nishioka, and Y. Shinoda, J. Appl. Phys. **54**, 5466–5470 (1983).
[48]V. Selvamanickam, S. Sambandam, A. Sundarama, S. Lee, A. Rar, X. Xiong, A. Alemu, C. Boney, and A. Freundlich, J. Cryst. Growth **311**, 4553–4557 (2009).
[49]S. Ruthberg, J. Res. Natl. Bur. Stand., Sect. A **67A**(6), 585–590 (1963).
[50]B. W. Sloope and C. O. Tiller, J. Appl. Phys. **33**(12), 3458–3463 (1962).
[51]M. Barkai, E. Grünbaum, and G. Deutscher, J. Vac. Sci. Technol. A. **9**(5), 2642–2647 (1991).
[52]L. Chen, W. Xie, G.-C. Wang, I. Bhat, S. Zhang, A. Goyal, and T.-M. Lu, Thin Solid Films **603**, 428–434 (2016).
[53]C. Gaire, P. Snow, T. L. Chan, W. Yuan, M. Riley, Y. Liu, S. B. Zhang, G.-C. Wang, and T.-M. Lu, Nanotechnology **21**(44), 445701 (2010).
[54]P. Snow, C. Gaire, T.-M. Lu, and G.-C. Wang, Thin Solid Films **519**(16), 5413–5418 (2011).
[55]L. Chen, T.-M. Lu, and G.-C. Wang, J. Appl. Phys. **112**, 024303 (2012).